Ensemble Effect in Bimetallic Electrocatalysts for CO_2 Reduction

Yuxuan Wang,[1,†] Liang Cao,[2,†] Nicole J. Libretto,[3] Xing Li,[4, 5] Chenyang Li,[2] Yidong Wan,[1] Connie He,[1] Jinsung Lee,[1] John Gregg,[1] Han Zong,[1] Dong Su,[4] Jeffery T. Miller,[3] Tim Mueller[2,*] and Chao Wang[1,*]

[1]Department of Chemical and Biomolecular Engineering and [2]Department of Materials Science and Engineering, Johns Hopkins University, Baltimore, Maryland 21218, United States;

[3]Davidson School of Chemical Engineering, Purdue University, West Lafayette, Indiana 47907, United States;

[4]Center for Functional Nanomaterials, Brookhaven National Laboratory, Upton, NY 11973, United States;

[5]Key Laboratory of Material Physics, Ministry of Education, Department of Physics and Engineering, Zhengzhou University, Zhengzhou, 450052, China.

† These authors contributed equally to this work.

* Email: chaowang@jhu.edu; tmueller@jhu.edu.

Abstract

Alloying is an important strategy for the design of catalytic materials beyond pure metals. The conventional alloy catalysts however lack precise control over the local atomic structures of active sites. Here we report on aninvestigation of the active site ensemble effect in bimetallic Pd-Au electrocatalysts for CO_2 reduction. A series of Pd@Au electrocatalysts are synthesized by decorating Au nanoparticles with Pd of controlled doses, giving rise to bimetallic surfaces containing Pd ensembles of various sizes. Their catalytic activity for reduction of CO_2 to CO exhibits a nonlinear behavior in dependence of the Pd content, which is attributed to the variation of Pd ensemble sizes and the corresponding tuning of adsorption properties. Density functional theory calculations reveal that the Pd@Au electrocatalysts with atomically dispersed Pd sites possess lower energy barriers for activation of CO_2 than pure Au and are also less poisoned by strongly binding *CO intermediates than pure Pd, with an intermediate ensemble size of active sites, such as Pd dimers, giving rise to the balance between these two rate-limiting factors and achieving the highest activity for CO_2 reduction.

Electroreduction of CO_2 powered by solar or wind electricity offers a sustainable approach toward valuable chemicals and fuels.[1-3] Among the various products that can be generated from CO_2 reduction, CO is of particular interest considering the market scale and economic viability.[3-6] It can either be directly applied as feedstock for the chemical industry[7-8] or further electrochemically reduced to hydrocarbon fuels.[9-11] Despite its promise, the energy conversion and chemical transformation efficiencies of CO_2 reduction are still largely limited by the lack of active and selective electrocatalysts.

The performance of CO_2 reduction electrocatalysts is generally restricted by the volcano-type dependence of catalytic activity on the binding energy of CO, which also scales with other reaction intermediates such as *COOH, *CHO or *COH.[12-14] On weakly binding metals such as Cu, Au and Ag, where hydrogen evolution is also suppressed due to the weak binding of *H, the reaction rate is primarily limited by the large barrier for the activation of CO_2, namely formation of *COOH (Scheme 1, case (a)). On the other side, metals such as Pt, Pd and Ni bind to CO strongly and can facilely activate CO_2, but they are subject to CO poisoning, leaving only undesired hydrogen evolution through the interstitial sites (Scheme 1, case (c)). Alloying represents a common approach toward advanced catalysts beyond pure metals, in which heteroatomic interactions can induce geometric and/or electronic effects to modify the surface adsorption properties and reactivities.[15-19] Bimetallic alloy catalysts such as Pd-Au have been studied for CO_2 reduction. For example, Zhu *et al.* investigated twisted Pd-Au alloy nanowires with an Au-enriched core and Pd-enriched shell.[20] Yuan *et al.* reported on thin Pd-Au alloy shells formed on Pd nanocubes by employing galvanic replacement reaction.[19] Albeit the observed catalytic enhancements, these studies mostly focus on correlating the alloy composition to the electrocatalytic performance. In random face-centered cubic (fcc) alloys, the tuning of bulk

composition does not necessarily warrant precise control over the surface atomic structures. If the alloy surface still comprises continuous ensembles of individual elements, the aforementioned limiting factors of monometallic catalysts could still be present. Fundamental understanding of, and thereby meticulous control over, the atomic structures of active sites thus becomes important for the development of bimetallic electrocatalysts for CO_2 reduction in order to achieve catalytic performances substantially superior to the monometallic ones.[21-24]

We report here a new strategy to enhance the efficiency of CO_2 reduction by engineering the ensemble size of active sites on bimetallic catalysts. We hypothesize that dispersion of strongly binding metal sites, such as Pd, on the surface of a weak binding metal, e.g., Au, can combine the advantages of the two metals, simultaneously lowering the energy barrier for CO_2 activation and mitigating *CO poisoning (Scheme 1, case (b)), and aim to develop fundamental understanding of the ensemble effects of Pd sites on the electrocatalytic performance. For validation of this hypothesis, we have synthesized a series of Pd@Au catalysts of various Pd dispersions by low-temperature reduction of a palladium salt with hydrogen, which has allowed for decorating Au nanoparticles with Pd atoms at precisely controlled doses and varying the average size of Pd ensembles on the bimetallic surfaces. These catalysts were subjected to systematic electrocatalytic studies to examine the ensemble effect in CO_2 reduction electrocatalysis. We have employed a combination of aberration-corrected high-angle annular dark-field scanning transmission electron microscopy (HAADF-STEM), electron energy loss spectroscopy (EELS), X-ray absorption spectroscopy (XAS) and X-ray photoelectron spectroscopy (XPS) to characterize these catalysts, with the derived atomically resolved structure information further correlated to the surface properties determined by electrochemical sorption measurements. Density functional theory (DFT)[25] calculations were then performed to simulate the bimetallic Pd-Au surfaces with various

Pd ensemble sizes and interpret the composition-dependent trends observed on the Pd@Au catalysts.

Au nanoparticles of 4-5 nm in diameter were first grown by reduction of gold (III) chloride hydrate ($HAuCl_4 \cdot xH_2O$) in an oleylamine solution by using borane tert-butylamine, which were then deposited on a carbon black support (Figure S1).[26] To decorate the nanoparticles with Pd, the Au/C mixture was dispersed in an aqueous solution of palladium chloride ($PdCl_2$), with hydrogen bubbled into this solution to reduce Pd (II) and deposit Pd^0 atoms (Figures S2 and S3). The employment of molecular hydrogen as a weak reducing agent and amine-based ligands that preferentially bind to Pd (as compared to Au)[27-29] allows for precise control over the dose and atomic ratio of Pd from 2% (denoted as $Pd_2@Au_{98}$) to 20% ($Pd_{20}@Au_{80}$) (Figure 1a, with more details of the synthesis provided in the Supporting Information). Compositions of the Pd@Au nanoparticles were analyzed and confirmed by using inductively coupled plasma optical emission spectroscopy (ICP-OES) and Energy-Dispersive X-Ray Spectroscopy (EDS) (Table S1). X-ray diffraction patterns (XRD) exhibit the peaks corresponding to a single face-centered cubic (*fcc*) phase (Figure S4). We have used element mapping based on high-angle annular dark-field scanning transmission microscopy (HAADF-STEM) and electron energy loss spectroscopy (EELS) to follow the structural evolution at increasing Pd doses (Figure 1b-e; see Figure S5 for line-scanning profiles and Figure S6 for post-reaction images). For $Pd_2@Au_{98}$ and $Pd_5@Au_{95}$, the map of Pd is dominated by scattered, discrete dots, corresponding to highly dispersed Pd sites decorated on the Au nanoparticle surface (Figures 1b and c). As the dose of Pd increases, continuous ensembles of Pd appear and form a semi-continuous layer (Figure 1d for $Pd_{10}@Au_{90}$). Ultimately, the Au nanoparticle becomes completely encapsulated with a Pd shell in the case of $Pd_{20}@Au_{80}$ (Figure 1e). At all doses, the Pd atoms reside primarily on the surface of the Au seeds, suggesting

that elemental diffusion was insignificant under the present synthesis conditions (nearly ambient conditions, with temperature not higher than 60 ^{o}C).[30-32] For comparison, monometallic Pd nanoparticles of similar particle sizes (~5 nm) were also prepared and deposited on similar carbon substrates, which was used as control in the electrocatalytic studies (Figure S7).

Atomic structures of the Pd@Au nanoparticles were also characterized by using X-ray absorption spectroscopy (XAS). X-ray absorption near edge structure (XANES) regions of the Pd@Au nanoparticles resemble those of metallic Au (Au foil, 11.919 keV) and Pd (Pd foil, 24.349 keV) at the Au L_3- and Pd K-edge, respectively (Figures 2a and b). Structural information about local atomic coordination was inferred by fitting the extended X-ray adsorption fine structure (EXAFS) spectra (Figures 2c and d, with the fitted structural parameters summarized in Table S2). The total coordination number (CN, including Au-Au and Au-Pd) of Au is determined to be ~8 for all the Pd@Au nanoparticles, which is also in line with the size for the Au seeds.[33] The coordination for Au is dominated by Au-Au bonding, with CN_{Au-Au} and CN_{Au-Pd} being nearly consistent at ~7 and ~1, respectively, for the four types of Pd@Au nanoparticles (Figure 2e). The insensitivity of Au coordination to the composition indicates that Pd was mostly decorated on the surface of the Au nanoparticles, in line with the observation of insignificant element diffusion from the STEM-based element mapping analysis. The preferential exposure of Pd on the nanoparticle surface is also confirmed by the smaller total CN (Pd-Pd plus Pd-Au) for Pd than that for Au, which increases from 5.3 for $Pd_5@Au_{95}$ to 7.6 for $Pd_{20}@Au_{80}$ (Table S2). CN_{Pd-Pd} increases from 1.5 to 4.2 while CN_{Pd-Au} remains in the range of 3.3 – 3.8 as the Pd loading increases from 5% to 20%, reflecting the lateral growth of surface Pd ensembles at higher Pd doses (Figure 2f). In the particular instance of $Pd_5@Au_{95}$, CN_{Pd-Au} is ~2.5 times larger than CN_{Pd-Pd}. Such preferential bonding to Au is strongly indicative of the atomic dispersion of Pd sites on the surface.[34] Based

on the observed trends, it is highly likely that the ratio CN_{Pd-Au}/CN_{Pd-Pd} can be even larger for $Pd_2@Au_{98}$, although we were not able to collect XAS spectra at the Pd K-edge in this case due to the very weak signals at such a low Pd dose. Combining the findings from XAS analyses and the observations from element mapping, we infer that the overgrown Pd is likely atomically dispersed on the surface of the Pd@Au nanoparticles, with the dispersion increasing at reduced Pd doses.[35-37] Notably, the atomic structures of Pd sites remains stable under the reaction conditions of CO_2 reduction (Table S3 and Figure S8).

Electrocatalytic performance of the Pd@Au nanoparticles for CO_2 reduction was evaluated in a gas-tight H-type electrolysis cell with 0.1 M of $KHCO_3$ being used as the electrolyte (see the Methods and Figures S9-S13 in the Supporting Information). Gas- and liquid-phase products were analyzed by using gas chromatograph-mass spectroscopy (GC-MS) and nuclear magnetic resonance (NMR) spectroscopy, respectively. Figure 3a summarizes the measured total geometric current densities (J_{tot}) for the Pd@Au catalysts, in comparison to monometallic Au and Pd. At the same mass loading of metals (~10 $\mu g_{Au+Pd}/cm^2_{geo}$) and similar particle sizes (~5 nm), the Pd-decorated Au nanoparticles deliver much larger J_{tot}. In the instance of -0.5 V (vs. the reversible hydrogen electrode, RHE; the same potential scale is used in the following discussion unless otherwise specified), $Pd_5@Au_{95}$ reaches ca. 2.0 mA/cm^2_{geo}, which is followed by $Pd_{10}@Au_{90}$ and $Pd_2@Au_{98}$. $Pd_{20}@Au_{80}$ has much lower values of J_{tot} that fall between Au and Pd throughout the potential range (from -0.3 to -0.8 V) investigated here. $Pd_5@Au_{95}$ is also the most active catalyst for CO_2 reduction, delivering an J_{CO2} (counting all the carbonaceous products) of up to 5.8 mA/cm^2_{geo} at -0.8 V, followed by 3.3 and 2.9 mA/cm^2_{geo} for $Pd_{10}@Au_{90}$ and $Pd_2@Au_{98}$, respectively (Figure 3b). The value of J_{CO2} achieved by $Pd_5@Au_{95}$ at this potential represents an improvement factor of 3 compared to Au and 21 compared to Pd.

CO is the primary product for the CO_2 reduction catalyzed by the Pd@Au electrocatalysts, albeit small amounts of formate also detected (Figures 3c and S6). Faradaic efficiencies (FEs) of the products vary with the electrode potential. For example, FE_{CO} of the Pd@Au electrocatalysts typically exhibits an increase from ca. -0.3 to -0.5 V, and then decrease at more negative potentials (Figure 3d). The former behavior can be attributed to the activation of CO_2, whereas the latter may not be simply ascribed to the CO_2 transport limitation, but probably owing to the kinetic competition between CO_2 reduction and hydrogen evolution.[38-40] As can be seen from Figure 3b, J_{CO2} (and correspondingly conversion of CO_2) still increases monotonically at more negative potentials in this region, without presenting the plateau that is commonly seen at diffusion limitations.[40-41] More intriguing trends uncovered for the CO_2 reduction on the Pd@Au electrocatalysts are the dependences of CO and formate selectivities on the atomic ratio of Pd. Both the Faradaic efficiency (FE_{CO}) and partial current density (J_{CO}) toward CO exhibit a nonlinear behavior as the atomic ratio of Pd increases (Figure 3e). $Pd_5@Au_{95}$ has the highest activity for the selective reduction of CO_2 to CO, with FE_{CO} and J_{CO} reaching ~80% and 1.6 mA/cm^2_{geo} and at -0.5 V. The corresponding mass activity (j_{CO}) achieves 178 A/g_{metal}, representing an improvement factor of ~4 as compared to the Au nanoparticles, which is also substantially superior to most of the CO_2 reduction electrocatalysts reported in the literature (Table S3). Furthermore, the electrocatalytic performance of $Pd_5@Au_{95}$ was found to be durable, with <15% loss in FE_{CO} or J_{tot} over 24 hours of continuous operation (see Figure S14, in contrast to the fast degradation in the case of Pd as shown in Figure S12). In comparison, pure Au (0% of Pd) has a J_{CO} of only 0.49 mA/cm^2_{geo} and pure Pd (100% Pd) has a J_{CO} of only 0.008 mA/cm^2_{geo} at this potential. On the other side, the selectivity toward formate exhibits a monotonic increase with the content of Pd in the Pd@Au catalysts. At -0.3 V, FE_{HCOO^-} increases from 9.8% for $Pd_5@Au_{95}$ to 56% for pure Pd,

corresponding to the rise of J_{HCOO^-} from 0.019 to 0.059 mA/cm$^2_{geo}$ mA/cm$^2_{geo}$ (Figure 3f). The production of formate was negligible on pure Au and $Pd_2@Au_{98}$.

From the above discussion, we can see that the decoration of Pd at low doses on the Au nanoparticles have made the activation of CO_2 more facile, with the catalytic activity rising as the Pd content increases. On the other side, the bimetallic nanoparticles with high doses of Pd unsurprisingly behave more like the pure Pd catalyst, which loses catalytic activity for CO_2 reduction and produces more formate (Pd is known for selective reduction of CO_2 to formate, but only at low overpotentials and small current densities[42]). We ascribe this dependence of electrocatalytic performance on the Pd dose to the tuning of Pd dispersion, which determines the adsorption properties and surface reactivity of the bimetallic catalysts. In the following discussion, we will elaborate this effect by performing electrochemical sorption measurements to probe the surface properties.

Figure 4a presents the cyclic voltammograms (CVs) recorded on the Pd@Au electrocatalysts in 0.1 M of $HClO_4$. Pd shows a broad peak at potentials below 0.4 V, which can be assigned to adsorption (and absorption) of hydrogen (Pd-H).[43] This feature nearly diminishes in all Pd@Au catalysts, resembling the case of Au. Both Pd and $Pd_{20}@Au_{80}$ exhibit an explicit peak in the cathodic scan, corresponding to the reduction of surface palladium oxides (Pd-O) formed in the anodic scan. The peak position for $Pd_{20}@Au_{80}$ has a positive shift of ~120 mV as compared to Pd. For the other Pd@Au catalysts, the Pd-O peak is almost invisible, albeit being at potentials close to that for $Pd_{20}@Au_{80}$. Au does not exhibit any redox peaks in the same potential region. The observations from the CVs suggest that the surrounding Au weakens the binding of hydrogen and oxygen on the Pd sites, with the extent of alteration increasing with the dispersion of Pd.

Similar trends were more explicitly revealed for *CO from the CO stripping measurements (Figure 4b; see the Supporting Information for the protocols). All of the Pd-containing electrocatalysts exhibit a peak around 0.95 V, corresponding to the oxidation of pre-adsorbed CO on the Pd sites, while the pattern recorded for Au is featureless in the same potential region. This behavior is in line with the much stronger binding of *CO on Pd than on Au.[29] It is observed that the Pd@Au catalysts with smaller ratios of Pd have lower peak intensities, suggesting the dependence of CO adsorption on the dispersion of Pd sites. Given the consistent catalyst loadings (~50 $\mu g_{Pd+Au}/cm^2_{geo}$) and similar particle sizes in the CO stripping measurements, the calculated charge associated with CO stripping varies from 2.64 μC for $Pd_2@Au_{98}$ to 182 μC for $Pd_{20}@Au_{80}$, versus 298 μC for pure Pd (Figures 4c). This trend does not only correlate to the coverage of Pd on the catalyst surface, but also indicates the change of CO binding strength with the dispersion of Pd sites. To elucidate the latter effect, we have calculated the CO adsorption coefficient (η_{CO}) by dividing the number of adsorbed CO molecules (estimated from the charge of CO stripping) with the number of Pd atoms (derived from ICP analysis for the compositions) for a given Pd@Au catalyst (see the Supporting Information for the details of calculation). For comparison, η_{CO} was also calculated for Pd, for which only surface atoms are taken into account considering preferential exposure of Pd on the surface of the Pd@Au catalysts. As shown in Figure 4d (also see Table S4), the Pd@Au nanoparticles with lower Pd contents also possess smaller values of η_{CO}, ranging from 0.23 for $Pd_{20}@Au_{80}$ to 0.02 for $Pd_2@Au_{98}$. These results thus suggest that the binding strength of CO decreases with the content of Pd in the bimetallic electrocatalysts, corresponding to the reduction of Pd ensemble size (Figures 1 and 2).

The uncovered ensemble effect in the Pd@Au electrocatalysts was understood by performing DFT calculations for the adsorption of *CO and *COOH, the key intermediates

involved in the CO_2 reduction reaction, on bimetallic (111) and (100) surfaces, which were identified as the exposed facets on the Wulff construction of *fcc* Au nanoparticles (details are provided in the Supporting Information). Figures 5a and S15 present the predicted configurations of *CO and *COOH adsorbed on the Pd@Au (111) and (100) surfaces with various Pd ensemble sizes, respectively. Such ensembles were found to be abundant on the Pd@Au nanoparticles at low Pd doses based on Wulff construction and Monte Carlo simulation (Figures S16 and S17; see the Supporting Information for more deetails of the computational method). The strongest binding sites for both *CO and *COOH were found to be on top of Pd in the case of the Pd monomer, resembling the situation on Au(111) and Au(100) where CO is adsorbed on top of Au atoms. In the case of Pd dimer, the most stable configuration on both facets becomes the bridge adsorption for *CO. For the Pd trimer, CO is adsorbed on the interstitial site on the (111) surface and bridge site on (100), similar to the corresponding Pd-skin and pure Pd surfaces. The calculated CO adsorption energies are located between the values on pure Au and Pd surfaces for all bimetallic surfaces except for the Pd-skin surfaces, on which the binding of CO is strengthened due to strain (Figure 5b and Tables S7-S8). The strength of CO binding decreases with reducing size of the Pd ensemble, which is consistent with the trend for the Pd@Au catalysts derived from the CO stripping measurements (Figure 4d). These findings indicate that the Pd ensembles at the atomic scale are less succeptible to CO poisoning than either a pure Pd surface or a Pd skin on pure Au surfaces. The stability of *COOH was also found to increase with Pd ensemble size, corresponding to lower overpotentials required for activation of CO_2. The scaling relationship between the adsorption energies of *COOH and *CO on the different types of catalyst surfaces (Figure 5c) provides an explanation for the volano-like behavior of the catalytic activity for reduction of CO_2 to CO with respect to the Pd content (Figure 3e). An intermediate size of Pd ensemble (e.g., Pd-

dimer) plausibly achieves a balance between the binding strengths of *CO and *COOH, giving rise to a relatively low energy barrier for activation of CO_2 but without being substantially poisoned by *CO (namely the case illustrated in Scheme 1b). Thereby surface enrichment of such atomically dispersed Pd sites on the Pd@Au nanoparticles could account for the observed nonlinear behavior of composition-dependent electrocatalytic performance (Figures S16 and S17).

In this work, we have synthesized a series of Pd@Au electrocatalysts by decorating Au nanoparticles with Pd of controlled doses. Their catalytic activity for reduction of CO_2 to CO was found to exhibit a nonlinear behavior in dependence of the Pd content, which was attributed to the varying *CO and *COOH adsorption energies on the Pd sites of various ensemble sizes. The bimetallic Pd-Au surfaces with discrete, atomically dispersed Pd ensembles possess lower energy barriers for activation of CO_2 than pure Au and are also less poisoned by strongly binding *CO intermediates than pure Pd, with Pd dimers likely achieving a balance of these two rate-limiting factors. Our work highlights fine tuning of the atomic structures of active sites for the development of advanced catalysts.

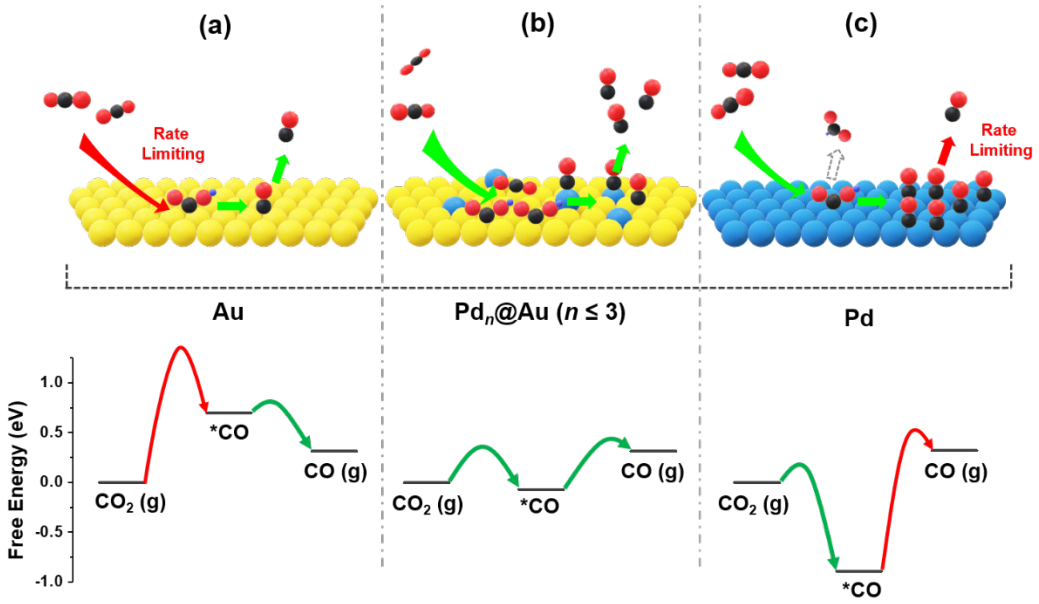

Scheme 1. Illustration of the concept using atomically dispersed Pd sites on Au surface to enhance CO_2 reduction. The yellow and blue spheres represent Au and Pd atoms, respectively. For the molecular structures, red, gray and purple colors represent oxygen, carbon and hydrogen, respectively. The red (versus green) arrows represent the rate-limiting factors in the reaction kinetics.

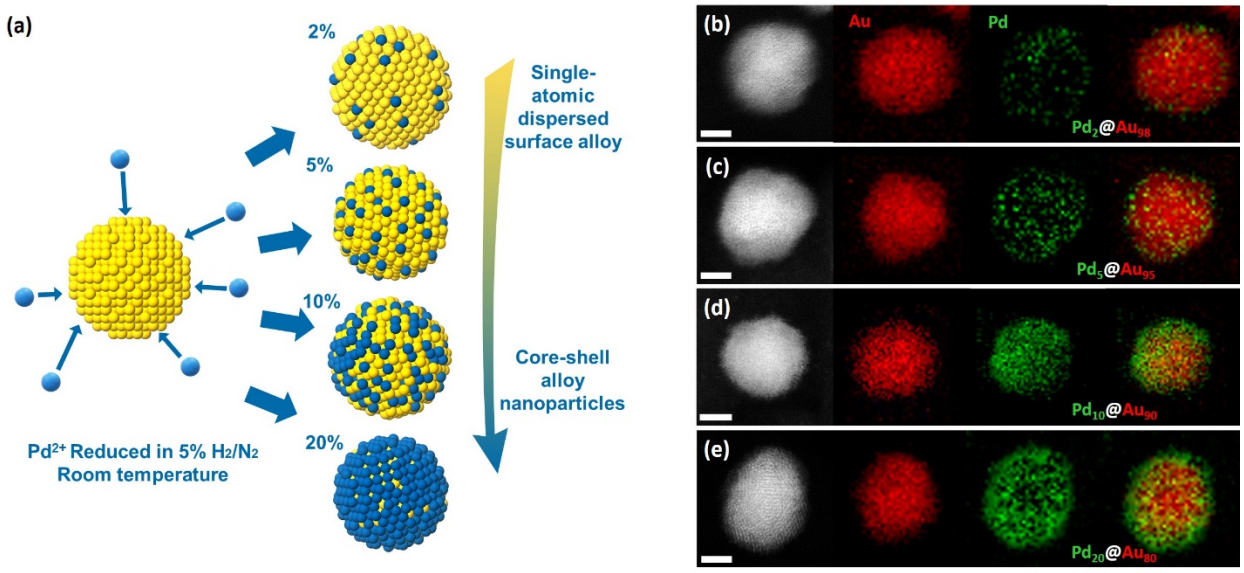

Figure 1. Synthesis and HAADF-STEM images of the Pd@Au nanoparticles. (a) Illustration of the synthetic scheme for the Pd@Au nanoparticles with control over the dose of Pd. (b-d) STEM images and EELS-based element maps for (b) $Pd_2@Au_{98}$, (c) $Pd_5@Au_{95}$, (d) $Pd_{10}@Au_{90}$ and (e) $Pd_{20}@Au_{80}$, where Au and Pd atoms are represented by red and green pixels, respectively.

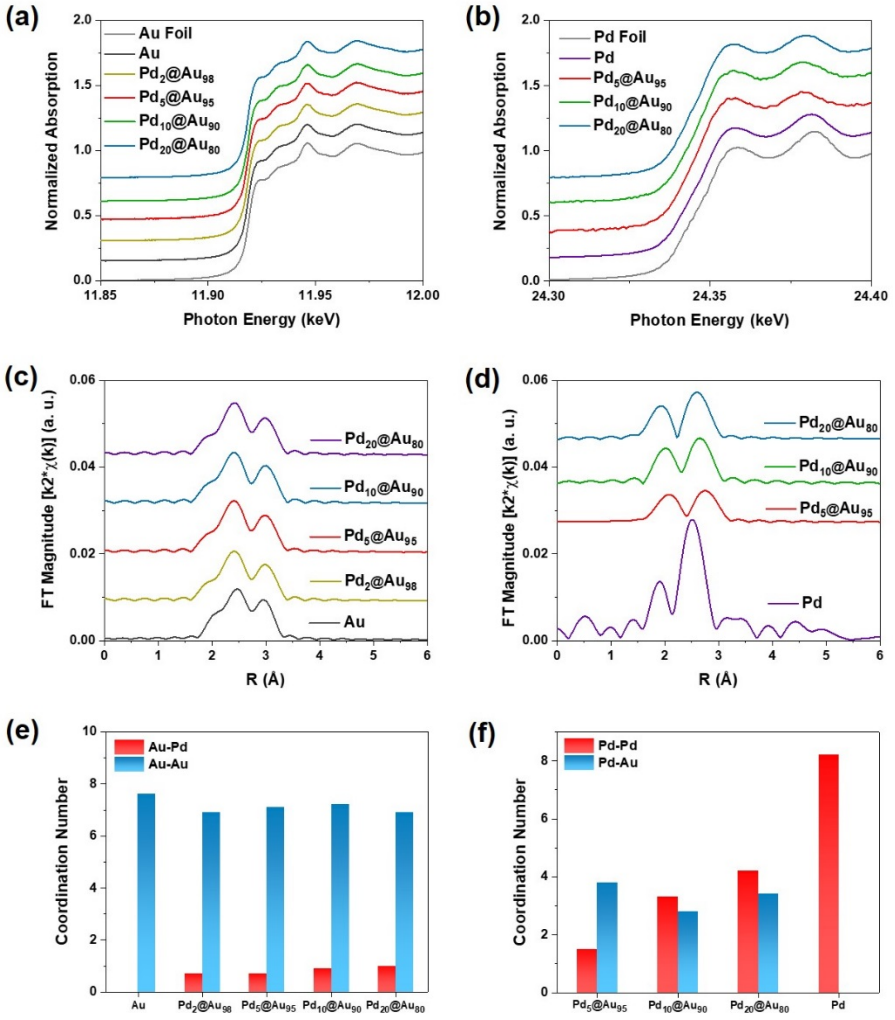

Figure 2. X-ray absorption spectroscopy (XAS) analysis for the Pd@Au nanoparticles. (a, b) XANES spectra at the Au L-edge (a) and the Pd K-edge (b). (c, d) k^2-weighted Fourier transform spectra at the Au L-edge (c) and the Pd K-edge (d). (e, f) Summary of coordination numbers (CNs) derived from the EXAFS analysis for Au (e) and Pd (f) atoms.

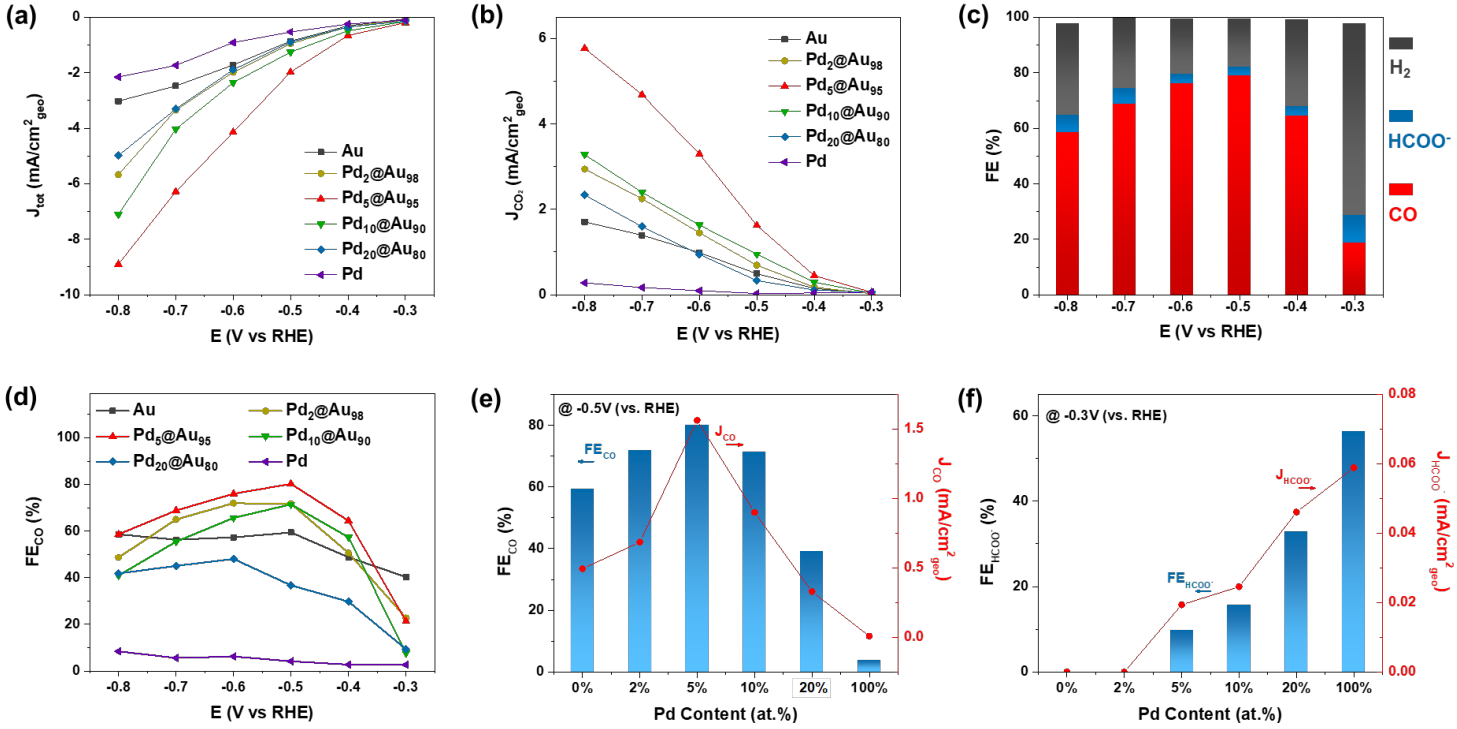

Figure 3. Performance of the Pd@Au electrocatalysts for CO_2 reduction. (a) Total electrode current density (J_{tot}). (b) CO_2 reduction current density (J_{CO2}) with all the carbonaceous products taken into account. (c) Faradaic efficiencies (FEs) of the different products determined for $Pd_5@Au_{95}$. (d) Comparison of FE toward CO (FE_{CO}) for the different electrocatalysts. (e) Dependences of FE_{CO} and partial current density toward CO (J_{CO}) (at -0.5 V) on the Pd content within the Pd@Au nanoparticles. (f) Dependences of Faradaic efficiency (FE_{HCOO^-}) and partial current density (J_{HCOO^-}) toward formate (at -0.3 V) on the Pd content within the Pd@Au nanoparticles.

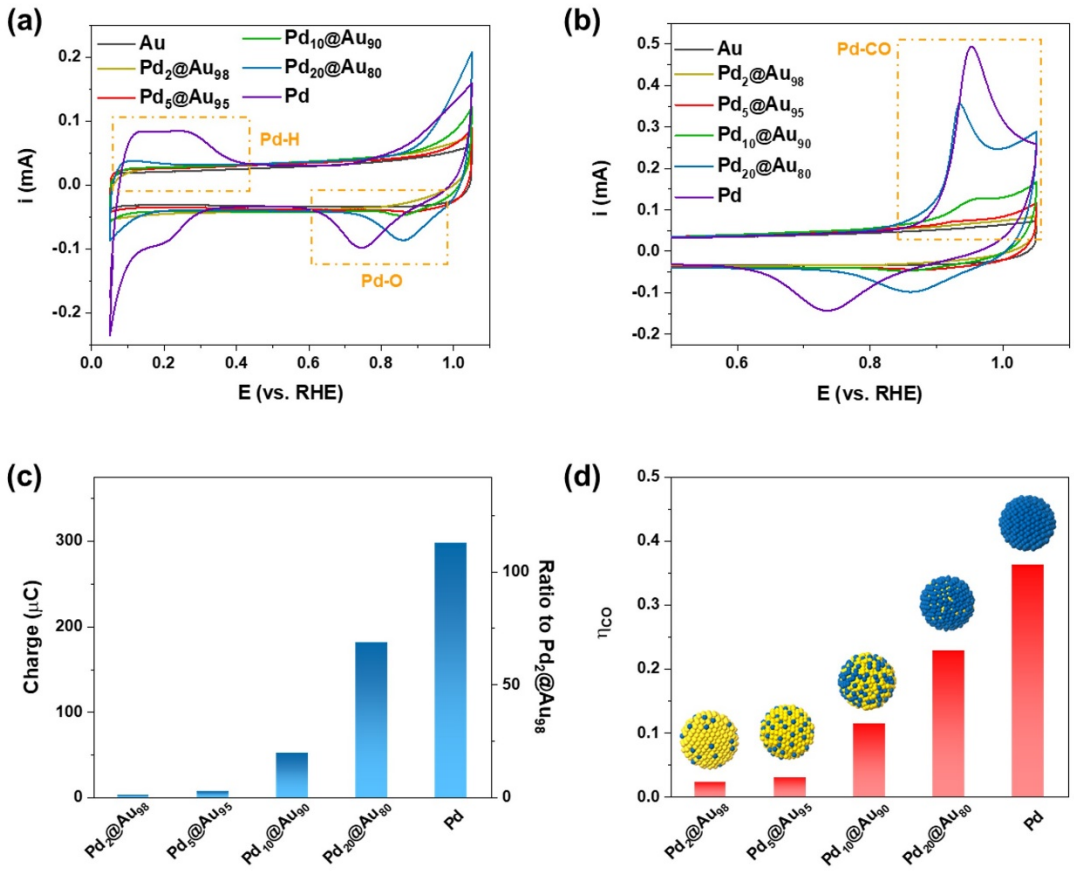

Figure 4. Electrochemical sorption measurements for probing the surface properties of Pd@Au. (a) Cyclic voltammograms (CVs) and (b) CO stripping patterns recorded on the different electrocatalysts (in 0.1 M of $HClO_4$, with a scanning rate of 50 mV/s). (c) Comparison of the calculated CO stripping charges. (d) Comparison of CO adsorption coefficient (η_{CO}) estimated for the Pd-based electrocatalysts.

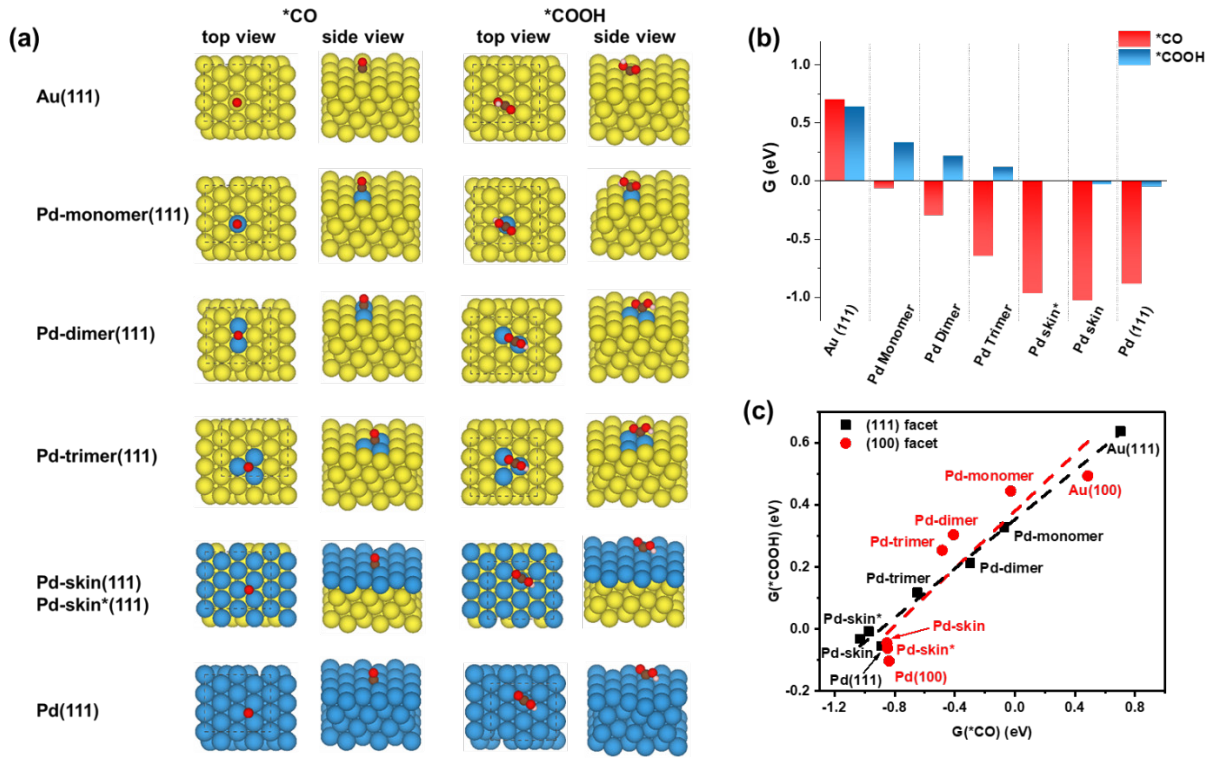

Figure 5. DFT calculations for the adsorption properties of Pd@Au bimetallic (111) and (100) surfaces with various Pd ensemble sizes. (a) Configurations of *CO and *COOH at the strongest binding sites on (111) surfaces. (b) Histograms summarizing the adsorption energies of *CO and *COOH on the different types of (111) surfaces. (c) Linear scaling relationship between the binding strengths of *CO and *COOH for both (111) and (100) surfaces. In (c) the black (R^2 = 0.98) and red (R^2 = 0.83) dashed lines are fitted for (111) and (100) surfaces, respectively. "Pd-skin" represents a monolayer of Pd on a pure Au surface with the Au lattice parameter, and "Pd-skin*" represents a monolayer of Pd on Au with the lattice parameter determined by the composition of $Pd_{20}@Au_{80}$ using Vegard's law.

ASSOCIATED CONTENT

Supporting Information

Detailed methods (synthesis, characterization, electrochemistry and DFT calculations) and corresponding additional data are provided in the Supporting Information.

AUTHOR INFORMATION

Corresponding Authors

*Email: chaowang@jhu.edu

*Email: tmueller@jhu.edu

Author Contributions

†Y.W. and L.C. contributed equally. C.W. conceived and oversaw the experimental work. Y.W., with the assistance of Y.W., C.H., J.L., J.G. and H.Z., performed the catalyst preparation, characterization and electrocatalytic studies. T.M. conceived and oversaw the computational work. L.C., with the assistance of C.L., conducted the DFT calculations on different Pd-Au surfaces and Monte Carlo simulations. X.L. and D.S. conducted the STEM examinations. N.L. and J.M. performed the XAS study. The authors acknowledge Prof. Tyrel McQueen (Dept. of Chemistry, JHU) and his student Hector Vivanco for assistance on XRD analysis. The manuscript was written through contributions of all authors. All authors have given approval to the final version of the manuscript.

Notes

The authors declare no competing financial interest.

ACKNOWLEDGEMENTS

This work was supported by the National Science Foundation (DMREF-1437396 and CBET-1803482) and the Johns Hopkins University Discovery Award. This study made use of the Johns Hopkins University Department of Chemistry Core Facilities and the authors would like to acknowledge the NMR manager Dr. Joel A. Tang for his assistance. T.M. and C.L. acknowledge the computational resources provided by XSEDE through NSF award DMR-140068, and by the Maryland Advanced Research Computing Center (MARCC). Atomic-scale structural images were generated using VESTA.[44] NJL and JTM were supported as part of the Center for Molecular Electrocatalysis, an Energy Frontier Research Center funded by the U.S. Department of Energy, Office of Science, Office of Basic Energy Sciences. This research used resources of the Advanced Photon Source, a U.S. Department of Energy (DOE) Office of Science User Facility operated for the DOE Office of Science by Argonne National Laboratory under Contract No. DE-AC02-06CH11357. MRCAT operations, beamline 10-BM are supported by the Department of Energy and the MRCAT member institutions. This research also used electron microscopy resources of the Center for Functional Nanomaterials, which is a U.S. DOE Office of Science Facility, at Brookhaven National Laboratory under Contract No. DE-SC001270.

REFERENCES

1. Appel, A. M.; Bercaw, J. E.; Bocarsly, A. B.; Dobbek, H.; DuBois, D. L.; Dupuis, M.; Ferry, J. G.; Fujita, E.; Hille, R.; Kenis, P. J. A.; Kerfeld, C. A.; Morris, R. H.; Peden, C. H. F.; Portis, A. R.; Ragsdale, S. W.; Rauchfuss, T. B.; Reek, J. N. H.; Seefeldt, L. C.; Thauer, R. K.; Waldrop, G. L., Frontiers, Opportunities, and Challenges in Biochemical and Chemical Catalysis of CO_2 Fixation. *Chem. Rev.* **2013,** *113* (8), 6621-6658.

2. Olah, G. A.; Prakash, G. K. S.; Goeppert, A., Anthropogenic Chemical Carbon Cycle for a Sustainable Future. *J. Am. Chem. Soc.* **2011,** *133* (33), 12881-12898.

3. Whipple, D. T.; Kenis, P. J. A., Prospects of CO_2 Utilization via Direct Heterogeneous Electrochemical Reduction. *J. Phys. Chem. Lett.* **2010,** *1* (24), 3451-3458.

4. Verma, S.; Kim, B.; Jhong, H.; Ma, S. C.; Kenis, P. J. A., A Gross-Margin Model for Defining Technoeconomic Benchmarks in the Electroreduction of CO_2. *Chemsuschem* **2016,** *9* (15), 1972-1979.

5. Jouny, M.; Luc, W.; Jiao, F., General Techno-Economic Analysis of CO_2 Electrolysis Systems. *Ind. Eng. Chem. Res.* **2018,** *57* (6), 2165-2177.

6. Bushuyev, O. S.; De Luna, P.; Dinh, C. T.; Tao, L.; Saur, G.; van de Lagemaat, J.; Kelley, S. O.; Sargent, E. H., What Should We Make with CO_2 and How Can We Make It? *Joule* **2018,** *2* (5), 825-832.

7. Jhong, H.-R. M.; Ma, S.; Kenis, P. J. A., Electrochemical conversion of CO_2 to useful chemicals: current status, remaining challenges, and future opportunities. *Curr. Opin. Chem. Engin.* **2013,** *2* (2), 191-199.

8. Ross, M. B.; Dinh, C. T.; Li, Y.; Kim, D.; De Luna, P.; Sargent, E. H.; Yang, P., Tunable Cu Enrichment Enables Designer Syngas Electrosynthesis from CO_2. *J. Am. Chem. Soc.* **2017,** *139* (27), 9359-9363.

9. Wang, Y.; Raciti, D.; Wang, C., High-Flux CO Reduction Enabled by Three-Dimensional Nanostructured Copper Electrodes. *ACS Catal.* **2018,** *8* (7), 5657-5663.

10. Li, C. W.; Ciston, J.; Kanan, M. W., Electroreduction of carbon monoxide to liquid fuel on oxide-derived nanocrystalline copper. *Nature* **2014,** *508* (7497), 504-507.

11. Jouny, M.; Luc, W.; Jiao, F., High-rate electroreduction of carbon monoxide to multi-carbon products. *Nat. Catal.* **2018,** *1* (10), 748-755.

12. Peterson, A. A.; Norskov, J. K., Activity Descriptors for CO_2 Electroreduction to Methane on Transition-Metal Catalysts. *J. Phys. Chem. Lett.* **2012,** *3* (2), 251-258.

13. Hori, Y., Electrochemical CO_2 Reduction on Metal Electrodes. In *Modern Aspects of* Electrochemistry; Springer: New York, NY, **2008,** Vol. 42, pp 89-189.

14. Kuhl, K. P.; Hatsukade, T.; Cave, E. R.; Abram, D. N.; Kibsgaard, J.; Jaramillo, T. F., Electrocatalytic Conversion of Carbon Dioxide to Methane and Methanol on Transition Metal Surfaces. *J. Am. Chem. Soc.* **2014,** *136* (40), 14107-14113.

15. Burch, R., Importance Of Electronic Ligand Effects In Metal Alloy Catalysts. *Acc. Chem. Res.* **1982,** *15* (1), 24-31.

16. Liu, P.; Norskov, J. K., Ligand and ensemble effects in adsorption on alloy surfaces. *Phys. Chem. Chem. Phys.* **2001,** *3* (17), 3814-3818.

17. Strasser, P.; Koh, S.; Anniyev, T.; Greeley, J.; More, K.; Yu, C.; Liu, Z.; Kaya, S.; Nordlund, D.; Ogasawara, H.; Toney, M. F.; Nilsson, A., Lattice-strain control of the activity in dealloyed core-shell fuel cell catalysts. *Nat. Chem.* **2010,** *2* (6), 454-60.

18. Wang, L.; Zeng, Z. H.; Gao, W. P.; Maxson, T.; Raciti, D.; Giroux, M.; Pan, X. Q.; Wang, C.; Greeley, J., Tunable intrinsic strain in two-dimensional transition metal electrocatalysts. *Science* **2019,** *363* (6429), 870-874.

19. Yuan, X.; Zhang, L.; Li, L.; Dong, H.; Chen, S.; Zhu, W.; Hu, C.; Deng, W.; Zhao, Z.-J.; Gong, J., Ultrathin Pd–Au Shells with Controllable Alloying Degree on Pd Nanocubes toward Carbon Dioxide Reduction. *J. Am. Chem. Soc.* **2019,** *141* (12), 4791-4794.

20. Zhu, S.; Wang, Q.; Qin, X.; Gu, M.; Tao, R.; Lee, B. P.; Zhang, L.; Yao, Y.; Li, T.; Shao, M., Tuning Structural and Compositional Effects in Pd–Au Nanowires for Highly Selective and Active CO_2 Electrochemical Reduction Reaction. *Adv. Energy Mater.* **2018,** *8* (32), 1802238.

21. Karamad, M.; Tripkovic, V.; Rossmeisl, J., Intermetallic Alloys as CO Electroreduction Catalysts-Role of Isolated Active Sites. *ACS Catal.* **2014,** *4* (7), 2268-2273.

22. Cheng, M. J.; Clark, E. L.; Pham, H. H.; Bell, A. T.; Head-Gordon, M., Quantum Mechanical Screening of Single-Atom Bimetallic Alloys for the Selective Reduction of CO_2 to C_1 Hydrocarbons. *ACS Catal.* **2016,** *6* (11), 7769-7777.

23. Greiner, M. T.; Jones, T. E.; Beeg, S.; Zwiener, L.; Scherzer, M.; Girgsdies, F.; Piccinin, S.; Armbrüster, M.; Knop-Gericke, A.; Schlögl, R., Free-atom-like d states in single-atom alloy catalysts. *Nat. Chem.* **2018,** *10* (10), 1008-1015.

24. Jiao, J.; Lin, R.; Liu, S.; Cheong, W.-C.; Zhang, C.; Chen, Z.; Pan, Y.; Tang, J.; Wu, K.; Hung, S.-F.; Chen, H. M.; Zheng, L.; Lu, Q.; Yang, X.; Xu, B.; Xiao, H.; Li, J.; Wang, D.; Peng, Q.; Chen, C.; Li, Y., Copper atom-pair catalyst anchored on alloy nanowires for selective and efficient electrochemical reduction of CO_2. *Nat. Chem.* **2019,** *11* (3), 222-228.

25. Kohn, W.; Sham, L. J., Self-Consistent Equations Including Exchange and Correlation Effects. *Phys. Rev.* **1965,** *140* (4A), A1133-A1138.

26. Peng, S.; Lee, Y. M.; Wang, C.; Yin, H. F.; Dai, S.; Sun, S. H., A Facile Synthesis of Monodisperse Au Nanoparticles and Their Catalysis of CO Oxidation. *Nano Res.* **2008,** *1* (3), 229-234.

27. Wu, B.; Zheng, N., Surface and interface control of noble metal nanocrystals for catalytic and electrocatalytic applications. *Nano Today* **2013,** *8* (2), 168-197.

28. Liu, R.; Zhang, L.-Q.; Yu, C.; Sun, M.-T.; Liu, J.-F.; Jiang, G.-B., Atomic-Level-Designed Catalytically Active Palladium Atoms on Ultrathin Gold Nanowires. *Adv. Mater.* **2016,** *29* (7), 1604571.

29. Gao, F.; Goodman, D. W., Pd–Au bimetallic catalysts: understanding alloy effects from planar models and (supported) nanoparticles. *Chem. Soc. Rev.* **2012,** *41* (24), 8009-8020.

30. Jirkovský, J. S.; Panas, I.; Ahlberg, E.; Halasa, M.; Romani, S.; Schiffrin, D. J., Single Atom Hot-Spots at Au–Pd Nanoalloys for Electrocatalytic H_2O_2 Production. *J. Am. Chem. Soc.* **2011,** *133* (48), 19432-19441.

31. Fang, Y.-L.; Miller, J. T.; Guo, N.; Heck, K. N.; Alvarez, P. J. J.; Wong, M. S., Structural analysis of palladium-decorated gold nanoparticles as colloidal bimetallic catalysts. *Catalysis Today* **2011,** *160* (1), 96-102.

32. Smith, D.; Petford-Long, A. K.; Wallenberg, L. R.; Bovin, J. O., Dynamic atomic-level rearrangements in small gold particles. *Science* **1986,** *223* (4766), 872-785.

33. Miller, J. T.; Kropf, A. J.; Zha, Y.; Regalbuto, J. R.; Delannoy, L.; Louis, C.; Bus, E.; van Bokhoven, J. A., The effect of gold particle size on AuAu bond length and reactivity toward oxygen in supported catalysts. *J. Catal.* **2006,** *240* (2), 222-234.

34. Duchesne, P. N.; Li, Z. Y.; Deming, C. P.; Fung, V.; Zhao, X. J.; Yuan, J.; Regier, T.; Aldalbahi, A.; Almarhoon, Z.; Chen, S. W.; Jiang, D. E.; Zheng, N. F.; Zhang, P., Golden single-atomic-site platinum electrocatalysts. *Nat. Mater.* **2018,** *17* (11), 1033-1039.

35. Shan, J. J.; Zhang, S. R.; Choksi, T.; Nguyen, L.; Bonifacio, C. S.; Li, Y. Y.; Zhu, W.; Tang, Y.; Zhang, Y. W.; Yang, J. C.; Greeley, J.; Frenkel, A. I.; Tao, F., Tuning Catalytic Performance through a Single or Sequential Post Synthesis Reaction(s) in a Gas Phase. *ACS Catal.* **2017,** *7* (1), 191-204.

36. Qiao, B. T.; Wang, A. Q.; Yang, X. F.; Allard, L. F.; Jiang, Z.; Cui, Y. T.; Liu, J. Y.; Li, J.; Zhang, T., Single-atom catalysis of CO oxidation using Pt_1/FeO_x. *Nat. Chem.* **2011,** *3* (8), 634-641.

37. Lucci, F. R.; Liu, J. L.; Marcinkowski, M. D.; Yang, M.; Allard, L. F.; Flytzani-Stephanopoulos, M.; Sykes, E. C. H., Selective hydrogenation of 1,3-butadiene on platinum-copper alloys at the single-atom limit. *Nat. Commun.* **2015,** *6,* 8550.

38. Ooka, H.; Figueiredo, M. C.; Koper, M. T. M., Competition between Hydrogen Evolution and Carbon Dioxide Reduction on Copper Electrodes in Mildly Acidic Media. *Langmuir* **2017,** *33* (37), 9307-9313.

39. Ren, D.; Fong, J. H.; Yeo, B. S., The effects of currents and potentials on the selectivities of copper toward carbon dioxide electroreduction. *Nat. Commun.* **2018,** *9,* 825.

40. Raciti, D.; Mao, M.; Park, J. H.; Wang, C., Mass transfer effects in CO_2 reduction on Cu nanowire electrocatalysts. *Cata. Sci. Tech.* **2018,** *8* (9), 2364-2369.

41. Singh, M. R.; Goodpaster, J. D.; Weber, A. Z.; Head-Gordon, M.; Bell, A. T., Mechanistic insights into electrochemical reduction of CO_2 over Ag using density functional theory and transport models. *Proc. Natl. Acad. Sci.* **2017,** *114* (42), E8812-E8821.

42. Kortlever, R.; Peters, I.; Koper, S.; Koper, M. T. M., Electrochemical CO_2 Reduction to Formic Acid at Low Overpotential and with High Faradaic Efficiency on Carbon-Supported Bimetallic Pd–Pt Nanoparticles. *ACS Catal.* **2015,** *5* (7), 3916-3923.

43. Zalineeva, A.; Baranton, S.; Coutanceau, C.; Jerkiewicz, G., Octahedral palladium nanoparticles as excellent hosts for electrochemically adsorbed and absorbed hydrogen. *Science Advances* **2017,** *3* (2).

44. Momma, K.; Izumi, F., VESTA: a three-dimensional visualization system for electronic and structural analysis. *J. Appl. Crystallogr.* **2008,** *41* (3), 653-658.